Limits for Absorption and Scattering by Core-Shell Nanowires in the Visible Spectrum

Aivar Abrashuly and Constantinos Valagiannopoulos[*]

Department of Physics, School of Science and Technology, Nazarbayev University, 53 Qabanbay Batyr Avenue, Astana, 010000, Kazakhstan

Testing the limits in performance of device setups with respect to sizes and oscillation frequencies by trying every single combination of the available media can give a set of superior designs with novel properties. This approach is followed for the absorption and scattering of visible light by core-shell nanowires, whose optical thickness is simultaneously large enough to individually perturb the background field and small enough to support coherent collective operation. Numerous maximally performing particles are reported, one for each pair of the bulk materials used, providing a set of limits for the absorbed and scattered power in the presence of realistic losses. This procedure detects the supported resonances at core-shell nanorods, finds the best designs for such a simple geometry, and thus offers additional degrees of freedom in particle or metasurface modeling.

I. INTRODUCTION

The way that particles react to incoming photonic beams can be expressed in terms of the power they absorb and the power they scatter in the background host [1]. Recently, with the advent of metasurfaces that use collectively numerous particles, the maximization of absorbed power or power scattered from them has attracted significant attention [2]. Power considerations of core-shell nanowires, in particular, are very popular and widely investigated due to their structural simplicity and analytical solvability. More specifically, extreme light absorption in thin semiconductor films wrapped around metallic rods has been reported [3] by optimization of the contribution from each angular-momentum channel and use of as many channels as possible. Moreover, excitation of the leaky modes of a single semiconducting cylinder can lead to tuning [4] of absorbed power for various incident angles, while significant absorption enhancement can be achieved in wire structures assisted by arrays of bowtie nanoantennas [5]. Similarly, scattering by infinite rods is an important effect that has been studied with use of coupled-mode theory [6,7]; accordingly, the alignment of various modes gives superscatterers, reaching the theoretical limits per channel [8].

An additional reason for the increasing popularity of the modeling, design, measurement, and testing of core-shell nanocylinders is the variety of their fabrication methods. The most-precise and most-expensive approach is the growth of semiconducting coats on metallic nanorods via molecule-by-molecule injection, as dictated by epitaxial deposition [9]. On the other hand, solution-processing techniques make feasible the wrapping [10] of plasmonic nanowires by oxide colloids with help from suitable chemical baths; in this way, the deposition is accomplished more easily and provides stable samples [11]. Finally, self-assembly mechanisms are a simple and robust way toward core-shell nanowires with controllable size and properties [12]; usually, patterned metallic cylinders are exposed to a suspension of inorganic particles, giving solid designs after drying in air [13].

Core-shell nanowires manufactured from inorganic media that support highly absorbing or scattering operations are extensively used in photovoltaics and several other applications. The geometry of nanorods enhances the effectiveness of charge collection by shortening the paths traveled by minority carriers [14] and provides the background host with exotic absorbing properties [15] that are particularly desirable in solar-cell designs [16]. For example, cylinders supporting morphology-dependent optical resonances exhibit high external quantum efficiency and pave the way to the development of ultrathin tunable optoelectronic devices comprising arrays of them [17]. Furthermore, similar nanotubes can be used as novel photodetectors with spectrally tuned absorption [18], ultrasensitive sensors in random networks of wires at the nanoscale [19], and modules of high-duality symmetry [20]. Finally, thermally sensitive scattering by core-shell cylinders in the terahertz regime enables controllable cloaking [21], while DNA-coated metallic rods can measure the length of molecules with subnanometer resolution [22].

---

[*]valagiannopoulos@gmail.com;
konstantinos.valagiannopoulos@nu.edu.kz

In this work, we systematically optimize elongated core-shell nanorods in terms of their absorption and scattering efficiency for numerous combinations of the available materials in the visible spectrum. The media used are chosen on the basis of the dispersive variation of their dielectric response to cover (in a coherent way) a substantial part of the complex-permittivity parametric space; a similar approach was successfully implemented for other objectives [23,24]. The physical size and the operating wavelength for every single case of the selected materials that gives maximal absorption or scattering are presented in the respective tables. We perform a brute-force search covering the entire visible spectrum, all the core-shell aspect ratios, and a specific range for electrical size allowing the particles to operate collectively. Since huge efficiencies are reported for extremely tiny objects [8] of restricted functionality, we reject maxima occurring at the lower limit of optical diameters and thus all the designs presented correspond to nonboundary extrema. It has been found that when an incident electric field is perpendicular to the cylinder's axis, optima occur for thicker and more-metallic designs that exhibit substantial robustness in absorbing and scattering both polarizations. It should also be stressed that most of the highly performing devices prefer plasmonic cores, with the exception of hollow metallic nanotubes, which change dramatically the near field within their ultrathin cladding. Such sharp variations in the field distribution can be used in wavefront-engineering applications; similarly, highly selective frequency responses exhibited by the reported nanorods are useful in filter or sensor modeling.

In this way, we report numerous optimal core-shell nanowires in the visible spectrum through a complete scanning of the parametric space by letting our metrics decide the best combination. The governing resonance effects are predicted and verified, while for each of the operations considered (absorption, scattering), several configurations with alternative materials are proposed to comply with additional potential constraints regarding ease of fabrication, availability, or packaging issues. The optimization approach tests the limits of a simplistic structural design in the presence of realistic losses, unlike other techniques reporting fundamental maxima regardless of the geometry [25,26]. However, we believe that the results presented offer additional degrees of freedom in metasurface patterning and the followed method contributes to the recent game-changing advances in inverse-design photonics [27, 28].

II. FORMULATION AND METHOD

A. Formulas and metrics

Consider a cylindrical particle possessing a core of radius a covered by cladding of thickness $(b - a)$ and normally illuminated by visible light in the form of a monochromatic TM_z or TE_z plane wave (z is the axis of the cylinder) that travels into free space [as in Fig. 1(a)]. The dispersive relative complex permittivities of the core ($r < a$) and the shell ($a < r < b$) are denoted by $\varepsilon_1 = \varepsilon_1(\omega)$ and $\varepsilon_2 = \varepsilon_2(\omega)$, respectively ($\omega$ is the operating frequency). The letters r, φ, and z are used for the related cylindrical coordinates, while the equivalent Cartesian ones are x, y, and z; the suppressed harmonic time is of the form $e^{i\omega t}$. Without loss of generality, we assume that the incident wave propagates along the $+x$ axis and its electric vector $\mathbf{E}_{\text{inc}}^{\text{TM}}$ (magnetic vector $\mathbf{H}_{\text{inc}}^{\text{TE}}$) is always parallel to the z axis for TM_z (TE_z) polarization, oscillating with unitary amplitude of 1 V/m (1 A/m). After imposition of the necessary boundary conditions, the scattered fields for $r > b$ (electric vector of TM_z set and magnetic vector for TE_z set, respectively) take the forms

$$\mathbf{E}_{\text{scat}}^{\text{TM}}/\mathbf{H}_{\text{scat}}^{\text{TE}} = \hat{\mathbf{z}} \sum_{n=-\infty}^{+\infty} S_n^{\text{TM/TE}} H_n(k_0 r) e^{in\varphi}, \quad (1)$$

where H_n is a Hankel function of the second kind of order n. In the following, we drop the subscript z from the TM/TE field characterization. Moreover, the scattering coefficients S_n are unitless and are not shown here for brevity [29]; obviously, the expression for $\mathbf{E}_{\text{scat}}^{\text{TM}}$ is multiplied by the incident 1 V/m and the corresponding expression for $\mathbf{H}_{\text{scat}}^{\text{TE}}$ is multiplied by 1 A/m. $k_0 = 2\pi/\lambda_0$ is the wavenumber in a vacuum.

The power (per unit length of the z axis) carried by the TM and TE scattered component in a vacuum expresses how much the presence of the cylinder changes the background field distribution external to it. Accordingly, P_{scat} can be easily computed with use of Poynting's theorem and expansions of $H_n(k_0 r)$ for large arguments $k_0 r \gg 1$ (in the far region), as follows [30]:

$$P_{\text{scat}}^{\text{TM/TE}} = W^{\text{TM/TE}} \sum_{n=-\infty}^{+\infty} \left| S_n^{\text{TM/TE}} \right|^2, \quad (2)$$

where $W^{\text{TM}} = (4/k_0\eta_0) \times (1 \text{ V/m})^2$ and $W^{\text{TE}} = (4\eta_0/k_0) \times (1 \text{ A/m})^2$, and η_0 is the free-space wave impedance. The power absorbed by the particle (again per unit length of the z axis), given the fact that one medium or both of the constituent media are lossy, is evaluated by application again of Poynting's theorem but for the total field into free space this time. If we integrate the power spatial density across any (normal-to-the-z-axis) circle of radius $r > b$ (even the infinite $k_0 r \to +\infty$ one), we obtain

$$P_{\text{abs}}^{\text{TM/TE}} = -P_{\text{scat}}^{\text{TM/TE}} - W^{\text{TM/TE}} \sum_{n=-\infty}^{+\infty} \text{Re}\left(i^n S_n^{\text{TM/TE}}\right). \quad (3)$$

Obviously, $P_{\text{scat}}, P_{\text{abs}} > 0$, which means that the series in Eq. (3) should converge to negative values smaller than

$-P_{\text{scat}}/W$. In the absence of any losses, we have $P_{\text{abs}} = 0$, and the aforementioned sum equals $-P_{\text{scat}}/W$.

To render the absorbed and scattered power more meaningful as magnitudes, we should normalize them with suitable quantities. For the first one, we can use as a reference parameter the power of the incident illumination passing through the physical cross section of the scatterer; namely, $P_{0,\text{abs}}^{\text{TM/TE}} = (k_0 b/2) W^{\text{TM/TE}}$. The ratio $P_{\text{abs}}/P_{0,\text{abs}}$ is equal to the absorption cross section [30] of the particle σ_{abs} (which is measured in meters) over the aperture of the rod as seen by the incoming plane wave ($2b$) for both polarizations. We normalize P_{scat} by the corresponding scattered power $P_{0,\text{scat}}$ from an impenetrable perfectly-electrically-conducting (PEC) cylinder with the same radius b. Since PEC surfaces reflect 100% of the incident field, it is a good choice to understand how more powerful is our scatterer against a relatively strong competitor. It should be stressed that our metric $P_{\text{scat}}/P_{0,\text{scat}}$ is 3–4 times smaller than the scattering cross section σ_{scat} expressed [30] in terms of the length $2b$ for the relatively thin wires considered in our study: $0.3 < k_0 b < 1.5$.

B. Optimization approach

Our aim is to consider a large set of available media for applications in the visible spectrum, 400 nm $< \lambda_0 <$ 700 nm, by taking into account their dispersive behavior. From this long list of materials, we wish to pick those combinations in suitably sized core-shell nanowires that overdeliver in terms of absorption and scattering. Our results could serve as a directory of maximal performances under the condition of using bulk media in simple two-layered structures. Alternatively, they can play the role of benchmarks for smarter designs to pass with respect to either structure [25] or texture (incorporating doped or artificial materials).

We follow a systematic approach that scans all the wavelengths λ_0 considered and for every one of them selects the configuration of dimensions (a, b) giving maximal $P_{\text{abs}}/P_{0,\text{abs}}$ or $P_{\text{scat}}/P_{0,\text{scat}}$ (for each polarization separately). In the optimization, we do not avoid homogeneous rods solely made of one material ($a/b \to 0, 1$) and thus $0 < a/b < 1$, while for the size of the nanowire we set an upper bound of a half wavelength and exclude [8] tiny structures ($0.05 < b/\lambda_0 < 0.25$). A typical contour of our metric P/P_0 on an $(a/b, b/\lambda_0)$ map is depicted in Fig. 1(b) at fixed λ_0. From several local maxima, we select the strongest one and we store it (together with the dimensions of the investigated design) as the best performance that can be achieved by a specific combination of materials for the oscillation wavelength λ_0 considered. The aforementioned global maximum corresponds to one point of the graph in Fig. 1(c) ($\lambda_0 = 600$ nm for that case), where the maximal P/P_0 for each wavelength is shown as function of λ_0. The quantity $\max_{\{0 < a/b < 1, 0.05\lambda_0 < b < 0.25\lambda_0\}} P/P_0$ is an outcome of

maximization, and thus the smooth behavior of Fig. 1(c) is not necessarily expected. From the graph in Fig. 1(c), we pick only one ultraperforming design for absorption or scattering with a certain frequency preference.

Unlike inequality $0 < a/b < 1$, which is imposed by the structure itself, the constraint $0.05 < b/\lambda_0 < 0.25$ is an artificial one, which inevitably affects the results obtained. In particular, extremely small sizes $b/\lambda_0 \to 0$ usually give very weak scatterers and absorbers; as has been indicated [8], no lower limit for b means that the best performance emerges for a resonant atom with an infinitesimal geometrical cross section. On the other hand, nanorods as big as λ_0 cannot serve as particles for collective operation in metasurfaces, arrays, and networks [31,32]. In the same context, when tiny particles are used, they can work only very close to each other, making a homogeneous layer, which loses the periodicity that gives metasurfaces their most-interesting properties [33]. On certain occasions, the largest value of P/P_0 in the rectangular plane in Fig. 1(b) is recorded for the low limit $b/\lambda_0 = 0.05$, which means that the true maximum is exhibited for a tiny particle outside the map considered. In such a case, we reject the solution and pick the secondary maximum, which is shorter but entirely in the parametric box considered. Therefore, the reported overdelivering structures always correspond to an internal (not boundary) extremum on the map in Fig. 1(b). Such a precaution in our optimization scheme makes the reported ultraperforming designs not substantially dependent on the lower limit of b/λ_0.

Our search for optimal designs examines several materials, including bulk metals, semiconductors, and inorganic dielectrics, whose permittivity profiles are obtained from a well-known material database [34] containing experimental data from well-established references [35,36]. The media are selected on the basis of their permittivity dispersion in the visible spectrum. Our intention is to cover as much of the parametric space for Re(ε) and Im(ε) as possible while the wavelength λ_0 is varied in the range from 400 to 700 nm. In the following, we assume that the dielectric constants ε_1 and ε_2 of our media remain the same at a specific wavelength λ_0, regardless of the sizes of their volume domains. Furthermore, the two materials in such a simple design should be chosen to be as different as possible [Re(ε_1)Re(ε_2) < 0] otherwise the conditions for interesting responses (various types of resonances) are not fulfilled. However, if a design uses a metallic coat, its plasmonic features in the visible spectrum create a huge impedance mismatch with the vacuum background, which usually isolates the inside volume. Therefore, from the available media, we conclude that the most-remarkable values related to absorption and scattering appear for a metallic core wrapped in a dielectric cladding [3]. By trying every single combination from our list of materials, we check the behavior of the device across all the operating wavelengths λ_0 and, through the
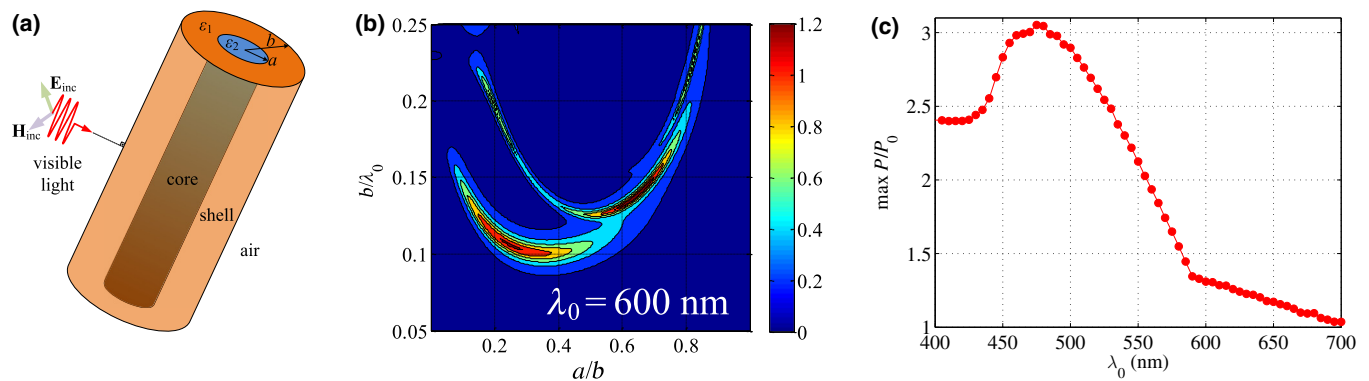
FIG. 1. (a) The structural model of the core-shell nanowire normally illuminated by a plane wave of visible light. (b) Typical variation of the metric P/P_0 (absorbed or scattered power divided by suitable normalization power) with respect to the aspect ratio a/b and the optical size b/λ_0 for prechosen materials and fixed wavelength. (c) Typical contour of maximal P/P_0 as a function of operating wavelength λ_0 for specific material selection.

optimization process described above, we chose a single design working at a specific frequency. In this way, we produce the tables presented herein, which contain the best cases corresponding to each core-shell pair of materials. It should be stressed that we may miss a highly performing design at a specific wavelength because a better one appears at another wavelength.

An important issue that should be clarified regarding how realistic is the structural model considered concerns the shape of the boundaries of the core and the shell when nanowires are actually fabricated. In practice, the cross sections of many dielectrics or semiconductors such as phosphides [37] or arsenides [38] have noncircular shapes such as hexagonal or triangular ones. However, our approximation for circular cylinders is sensible as long as the size of the particles is small compared with the operating wavelength, which is the case in this study. To put this another way, the (angular) state number of the supported mode is kept low [38] and thus the field developed across the nanowire only moderately "feels" the aforementioned imperfections of the shape.

As far as the underlying physical mechanism leading to optimal designs is concerned, it is well known that behind maximal-absorption and maximal-scattering operations in the aforementioned core-shell nanowires, two major types of resonances occur. The first type (thickness resonances) is the outcome of constructive interferences from oppositely propagating waves developed when light interacts with a finite-sized object [30]. The second type (plasmon resonances) concerns localized effects appearing at the surface between media with permittivities of opposite sign [15].

III. HIGHLY ABSORBING DESIGNS

In Table I, we give the highest-performing core-shell designs in terms of TM absorption when bulk media are

used; the working wavelength and the corresponding color of the spectrum are also shown. The maximal value of $P_{\text{abs}}^{\text{TM}}/P_{0,\text{abs}}^{\text{TM}}$ is around 2 (ranging from approximately 1.9 in InAs structures for multiple colors to approximately 2.4 in Ge-clad particles for red light). Furthermore, practically all the optimal designs correspond to moderately thick cylinders with electrical size $0.15 < 2b/\lambda_0 < 0.2$, which is mainly dictated by the external dielectric cladding regardless of the metal inside and the operating frequency. GaP-coated cylinders prefer to absorb violet light, while GaSb-coated and Ge-coated favor red light and suitable amorphous-silicon (a-Si) covers of metallic cylinders absorb orange light better for TM illumination. In contrast, AlSb-clad particles absorb very efficiently ($P_{\text{abs}}^{\text{TM}}/P_{0,\text{abs}}^{\text{TM}} > 2$) intermediate colors of the visible spectrum (blue, green). It is also remarkable that GaP alone does a better job in terms of TM absorption than any combination of silver-core designs; in that case, the plasmonic character of the metal does not help in establishing a resonance, and thus a single lossy rod attracts more energy from the background. Such a conclusion is compatible with other results [39] demonstrating that variants of GaP nanowires possess interesting optical properties. Finally, InAs-based nanowires exhibit substantial flexibility in terms of the frequency they absorb most; in particular, optimal λ_0 varies from green to orange wavelengths depending on what metal we use as a core.

In Table II, we present the corresponding optimally absorbing core-shell nanowires for TE illumination. On average, the values of $P_{\text{abs}}^{\text{TE}}/P_{0,\text{abs}}^{\text{TE}}$ are slightly lower than the ones in Table I but are for thicker structures (see especially particles with InAs covers). Indeed, in the TE case examined, the electric field that "feels" the permittivity discontinuity is oriented normal to the rod's axis and thus interacts with its cross section of width $2b$; that is why larger diameters are necessary, unlike in the TM polarization, where it "sees" the whole (infinite) cylinder

TABLE I.   Optimally-TM-absorbing core-shell nanowires. Performance $P_{abs}^{TM}/P_{0,abs}^{TM}$ at specific wavelengths λ_0 (indicated also by the corresponding color of the visible spectrum) and optimal material geometric sizes (a, b) for each combination of the available materials for which the proposed core-shell cylinder in Fig. 1(a) absorbs maximally the TM incident field. Each row corresponds to a different metallic core (ε_1) and each column corresponds to a different dielectric shell (ε_2).

	AlSb	*a*-Si	GaP	GaSb	Ge	InAs
Ag	2.09 at 505 nm	2.02 at 610 nm	1.92 at 400 nm	2.14 at 700 nm	2.26 at 700 nm	1.95 at 610 nm
	$b/\lambda_0 = 0.083$	$b/\lambda_0 = 0.093$	$b/\lambda_0 = 0.087$	$b/\lambda_0 = 0.088$	$b/\lambda_0 = 0.077$	$b/\lambda_0 = 0.100$
	$a/b = 0.37$	$a/b = 0.50$	$a/b = 0$	$a/b = 0.56$	$a/b = 0.41$	$a/b = 0.55$
Al	2.17 at 500 nm	2.12 at 620 nm	1.95 at 400 nm	2.19 at 700 nm	2.36 at 700 nm	1.97 at 565 nm
	$b/\lambda_0 = 0.087$	$b/\lambda_0 = 0.093$	$b/\lambda_0 = 0.089$	$b/\lambda_0 = 0.084$	$b/\lambda_0 = 0.078$	$b/\lambda_0 = 0.093$
	$a/b = 0.47$	$a/b = 0.44$	$a/b = 0.32$	$a/b = 0.47$	$a/b = 0.41$	$a/b = 0.49$
Au	2.10 at 500 nm	2.00 at 615 nm	2.04 at 400 nm	2.12 at 700 nm	2.25 at 700 nm	1.92 at 590 nm
	$b/\lambda_0 = 0.083$	$b/\lambda_0 = 0.092$	$b/\lambda_0 = 0.094$	$b/\lambda_0 = 0.088$	$b/\lambda_0 = 0.076$	$b/\lambda_0 = 0.100$
	$a/b = 0.44$	$a/b = 0.49$	$a/b = 0.55$	$a/b = 0.58$	$a/b = 0.39$	$a/b = 0.59$
Ti	2.23 at 525 nm	2.12 at 620 nm	2.14 at 400 nm	2.13 at 700 nm	2.36 at 700 nm	1.93 at 590 nm
	$b/\lambda_0 = 0.087$	$b/\lambda_0 = 0.089$	$b/\lambda_0 = 0.093$	$b/\lambda_0 = 0.079$	$b/\lambda_0 = 0.075$	$b/\lambda_0 = 0.090$
	$a/b = 0.45$	$a/b = 0.43$	$a/b = 0.51$	$a/b = 0.43$	$a/b = 0.38$	$a/b = 0.44$

length. For the same reason, smaller radius ratios a/b are required in the optimal designs in Table I compared with those in Table II because the longitudinally oscillating electric field needs a smaller volume from the stronger scatterer (metal) to establish a resonant regime. Furthermore, it is natural to have a trade-off between the optimal performance and the physical dimension since the normalization denominators $P_{0,abs}^{TM/TE}$ are proportional to the size $2b$ of the cylinder. As in Table I, Ge- and GaSb-coated metals absorb maximally the TE incident field for long visible wavelengths λ_0 (red color). However, this does not mean that these material combinations work efficiently for both polarizations simultaneously, since the optimal designs in Tables I and II are different (in radii a and b). The AlSb and GaP claddings can adapt their optimal operating frequency according to the metallic core. Finally, we mention

the Ag/GaP particle, which has moderate size but manages to absorb 3 times the incident power $P_{0,abs}^{TE}$ passing through its cross section.

In Fig. 2(a), we present the spatial distribution of the total (z) electric field magnitude for a representative design from Table I. Practically all the optimally-TM-absorbing structures exhibit concentration of the electric field close to their external surface at two antipodal positions of the x axis. The two hot spots correspond to oppositely directed electric fields completing a zero-crossing variation within the diameter of a particle. Such behavior reminds us of bipolar Mie resonances giving minimum denominators of the corresponding canonical series in cylindrical coordinates. In Fig. 2(b), we show the typical (x, y) dependence of the magnetic field for maximally-TE-absorbing designs from Table II. The substantial relative magnitude of the

TABLE II.   Optimally-TE-absorbing core-shell nanowires. Performance $P_{abs}^{TE}/P_{0,abs}^{TE}$ at specific wavelengths λ_0 (indicated also by the corresponding color of the visible spectrum) and optimal material geometric sizes (a, b) for each combination of the available materials for which the proposed core-shell cylinder in Fig. 1(a) absorbs maximally the TE incident field. Each row corresponds to a different metallic core (ε_1) and each column corresponds to a different dielectric shell (ε_2).

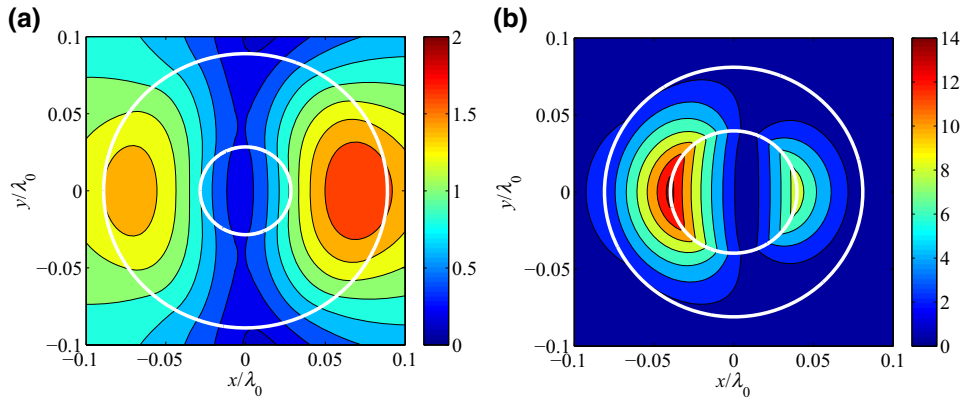|	AlSb	*a*-Si	GaP	GaSb	Ge	InAs
Ag	2.05 at 620 nm	1.87 at 590 nm	3.05 at 475 nm	1.91 at 700 nm	2.10 at 700 nm	1.72 at 565 nm
	$b/\lambda_0 = 0.081$	$b/\lambda_0 = 0.118$	$b/\lambda_0 = 0.051$	$b/\lambda_0 = 0.113$	$b/\lambda_0 = 0.103$	$b/\lambda_0 = 0.128$
	$a/b = 0.49$	$a/b = 0.75$	$a/b = 0.60$	$a/b = 0.74$	$a/b = 0.73$	$a/b = 0.77$
Al	2.07 at 565 nm	1.76 at 620 nm	1.98 at 425 nm	1.61 at 700 nm	1.80 at 700 nm	1.58 at 590 nm
	$b/\lambda_0 = 0.107$	$b/\lambda_0 = 0.119$	$b/\lambda_0 = 0.111$	$b/\lambda_0 = 0.122$	$b/\lambda_0 = 0.110$	$b/\lambda_0 = 0.210$
	$a/b = 0.52$	$a/b = 0.63$	$a/b = 0.64$	$a/b = 0.69$	$a/b = 0.68$	$a/b = 0.81$
Au	1.90 at 620 nm	1.76 at 590 nm	1.85 at 600 nm	1.88 at 700 nm	2.01 at 700 nm	1.65 at 565 nm
	$b/\lambda_0 = 0.081$	$b/\lambda_0 = 0.125$	$b/\lambda_0 = 0.084$	$b/\lambda_0 = 0.115$	$b/\lambda_0 = 0.107$	$b/\lambda_0 = 0.137$
	$a/b = 0.64$	$a/b = 0.81$	$a/b = 0.54$	$a/b = 0.77$	$a/b = 0.77$	$a/b = 0.84$
Ti	1.54 at 590 nm	1.34 at 620 nm	1.58 at 500 nm	1.25 at 700 nm	1.31 at 700 nm	1.26 at 590 nm
	$b/\lambda_0 = 0.128$	$b/\lambda_0 = 0.231$	$b/\lambda_0 = 0.138$	$b/\lambda_0 = 0.240$	$b/\lambda_0 = 0.127$	$b/\lambda_0 = 0.239$
	$a/b = 0.71$	$a/b = 0.87$	$a/b = 0.68$	$a/b = 0.89$	$a/b = 0.79$	$a/b = 0.87$

FIG. 2. Typical spatial distribution of the normalized magnitude of (a) the sole electric component for the optimally-TM-absorbing Al/GaP nanowire at $\lambda_0 = 400$ nm and (b) the sole magnetic component for the optimally-TE-absorbing Ag/AlSb nanowire at $\lambda_0 = 620$ nm. The boundaries are denoted by solid white lines.

signal recorded at the internal surface of the nanowire is attributed to the localized surface plasmon developed between the metal and the dielectric [40]. Again, the resonance is dipolar and two maxima of opposite signs are exhibited along the direction of incoming light (x).

For the far-field response, only the omnidirectional term (S_0) and the dipolar ($S_1 = -S_{-1}$) term are nonnegligible in most of the designs in Tables I and II. Therefore, the azimuthal profile of the scattered power takes the following form: $p(\varphi) \cong |S_0|^2 + 4|S_1|^2 \cos^2 \varphi + 4[\text{Im}(S_0)\text{Re}(S_1) - \text{Re}(S_0)\text{Im}(S_1)] \cos \varphi$. When the nanowires are working in the highly absorbing mode, most of them react like Huygens sources reflecting poorly the directly incident rays and responding strongly along the forward direction ($\varphi = 0$) to create the necessary shading [41]. Such a response results in a stronger field maximum for $x > 0$ (compared with that occurring for $x < 0$) into the TM nanowires, while it does not affect the signal into TE cylinders, which is concentrated internally around $x = \pm a$. However, few designs can absorb optimally while giving a dipolelike pattern if excited by TE waves; in particular, this occurs for the four thinnest cylinders in Table II (Ag/AlSb, Ag/GaP, Au/AlSb, and Au/GaP). Their behavior is attributed to the suppression of the omnidirectional term $|S_0|^2$ compared with the bipolar one $|S_1|^2$ and to the fact that the two complex numbers S_0 and S_1 are in phase or out of phase, leading to a vanishing $\cos \varphi$ term in $p(\varphi)$.

In all the previous examples, substantial $P_{\text{abs}}/P_{0,\text{abs}}$ is recorded for nanorods with a metallic core since otherwise the huge impedance discontinuity with the vacuum background will prevent the field from penetrating into the structure, as mentioned in Sec. II. However, we find that high absorbing performance can be achieved with thin, hollow metallic tubes of suitable dimensions under TE illumination. Since absorption occurs only within the lossy shell, the efficiency of the designs can be attributed to the pair of surface plasmons created along the two concentric cylindrical boundaries of the metallic tube. Since the size ($b - a$) of the shell is small, the field concentration at the external surface $r = b$ can feed also a surface plasmon at $r = a$; in this way, significant signal power is developed across the entire area of the plasmonic cover, which, due to its metallic losses $\text{Im}(\varepsilon_2)$, gives substantial absorption. In Fig. 3(a), we show the spatial distribution of total $\left| \mathbf{H}_{\text{inc}}^{\text{TE}} + \mathbf{H}_{\text{scat}}^{\text{TE}} \right|$ for the case of an optimal hollow silver tube, where a quadrupole near-field pattern is observed (the $S_{\pm 2}$ coefficients are of non-negligible magnitude). One can also notice the rapid change of the field into the thin metallic shell, which emulates an "effective discontinuity" of the signal between the outer vacuum region and the inner vacuum region [42]. Similar remarks can be made for Fig. 3(b), where aluminum plays the role of a plasmonic medium, with the difference that the particle is electrically larger, the quadrupole response is less obvious, and
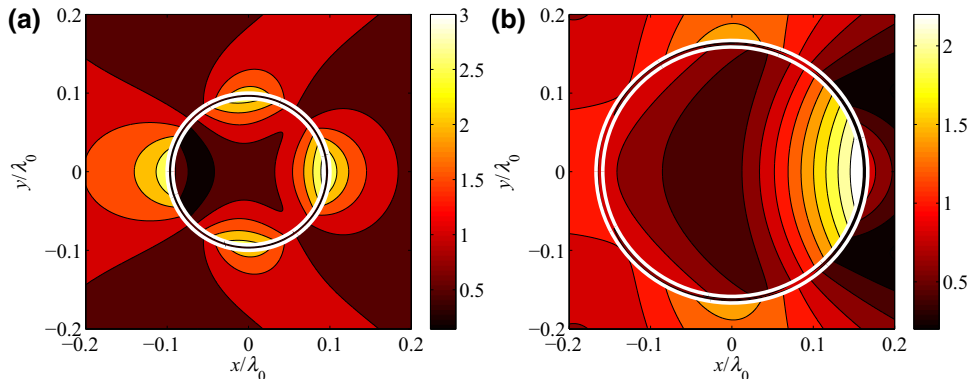

FIG. 3. Spatial distribution of the magnitude of the normalized sole magnetic component for the optimally-TE-absorbing hollow metallic tubes for (a) an empty silver shell at $\lambda_0 = 575$ nm ($P_{\text{abs}}/P_{0,\text{abs}} \cong 1.6$) and (b) an empty aluminum shell at $\lambda_0 = 495$ nm ($P_{\text{abs}}/P_{0,\text{abs}} \cong 1.4$).
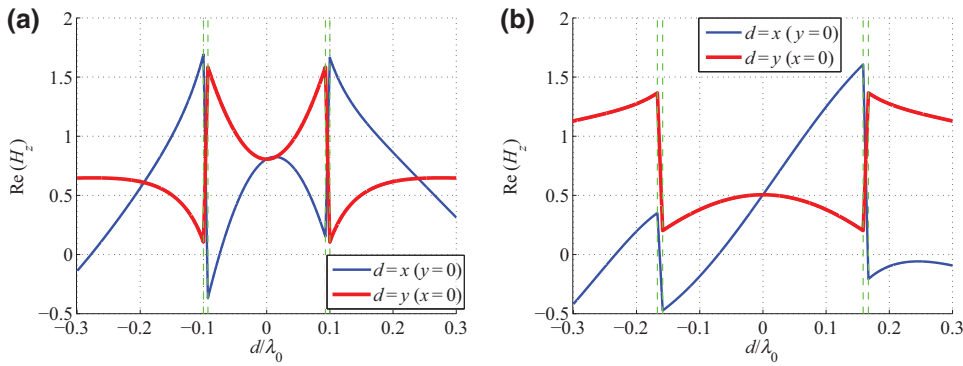
FIG. 4. Time snapshots of the normalized magnetic field along the lines $y = 0$ (blue) and $x = 0$ (red) as functions of x/λ_0 and y/λ_0, respectively, for (a) the empty silver shell in Fig. 3(a) and (b) the empty aluminum shell in Fig. 3(b). Dashed green lines represent the physical boundaries.

the variation of the field into the coating is more abrupt. Note that the TM absorption of the aforementioned metallic nanotubes in Fig. 3 is very low. An effect similar to the one shown in Fig. 3 indicated by our optimization has been attributed to excitation of hybrid antiphase localized plasmon supermodes [43].

In Fig. 4(a), we show linear plots of the algebraic value of the z-polarized magnetic field along normally crossed lines passing from the center of the particle in Fig. 3(a). Obviously, the vertical cross section of the field is an even function of y/λ_0, unlike the curve of the horizontal cross section, which is biased by the side of excitation. In both directions, we notice the linear and very sudden change of the signal within the metallic coat, whose thickness is less than 1% of the free-space wavelength. Far from the structure, we find the expected wavelike response with respect to x/λ_0 and substantial scattering perturbation with respect to y/λ_0. In Fig. 4(b), we show exactly the same quantities as in Fig. 4(a) but for the empty aluminum shell in Fig. 3(b). Again, the extremely abrupt variation within the thin cover makes the magnetic field along the x axis flip sign once it passes through it. Similarly, the sharp change of the signal along the y axis for $y \cong \pm a \cong \pm b$ demonstrates the aforementioned "effective discontinuity" at the plasmonic tube, which is related to its substantial texture contrast with a free-space environment.

It would also be meaningful to investigate some of the optimal designs when the working wavelengths are

not exactly equal to the ones given in Tables I and II. In Fig. 5(a), we consider six core-shell nanowires from Table I (each one operated at a different color of the visible spectrum indicated by the color of the curves) and representing the metric $P_{\text{abs}}/P_{0,\text{abs}}$ for both polarizations as a function of λ_0. Obviously, we obtain bell-like solid lines since the performance falls far from the central wavelength (the one indicated in Tables I and II), even if slightly better results may be achieved for neighboring frequencies due to discretization of continuous λ_0 space. Furthermore, as anticipated, the metric for TE illumination (dashed lines) is significantly reduced since the structures have not been optimized for waves of this type. It is, however, remarkable that most TE curves (except for the output of the Au/InAs design) are maximized almost at the same wavelengths at which the TM ones (solid lines) have their largest values; this happens despite the totally different nature of the two field polarizations for an infinite cylinder. Finally, the drop of the absorption efficiency may be more (Ti/GaP and Ti/AlSb particles) or less (Au/InAs and Ti/a-Si particles) abrupt, as dictated by the dispersive behavior of the media used.

In Fig. 5(b), we present curves similar to those in Fig. 5(a) for certain designs picked from Table II. For most of the particles, both of their curves (dashed lines for TE polarization and solid lines for TM polarization) possess substantial magnitudes in the vicinity of the central operating wavelengths. In particular, TM and TE
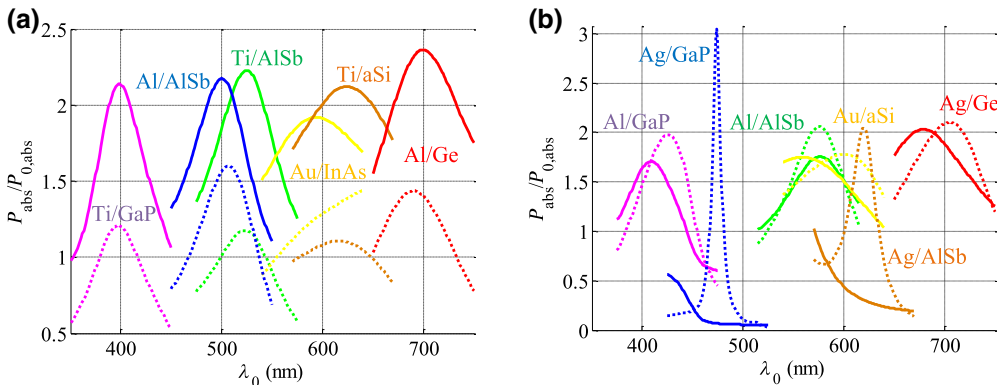

FIG. 5. Absorption efficiencies $P_{\text{abs}}/P_{0,\text{abs}}$ for both polarizations as a function of the operating wavelength λ_0 of selected optimal designs picked from (a) Table I and (b) Table II. Solid lines correspond to the TM response and dashed lines correspond to the TE response.

TABLE III.   Optimally scattering core-shell nanowires. Performance $P_{scat}/P_{0,scat}$ at specific wavelengths λ_0 (indicated also by the corresponding color of the visible spectrum) and optimal material geometric sizes (a, b) for each combination of the available materials for which the proposed core-shell cylinder in Fig. 1(a) scatters maximally the TM or TE incident field. Each column corresponds to a different metallic core (ε_1) and each row corresponds to a different dielectric shell (ε_2). Grey box indicate poor performance. $P_{0,scat}$ is the corresponding scattering power of an equal-sized PEC rod.

	Alone under TM waves	Ag under TM waves	Al under TM waves	Alone under TE waves	Ag under TE waves	Au under TE waves
AlSb	2.58 at 700 nm $b/\lambda_0 = 0.098$	2.62 at 700 nm $b/\lambda_0 = 0.099$ $a/b = 0.24$	2.58 at 700 nm $b/\lambda_0 = 0.098$ $a/b = 0$		1.83 at 700 nm $b/\lambda_0 = 0.188$ $a/b = 0.81$	1.64 at 700 nm $b/\lambda_0 = 0.194$ $a/b = 0.84$
GaP	2.81 at 480 nm $b/\lambda_0 = 0.101$	2.84 at 480 nm $b/\lambda_0 = 0.102$ $a/b = 0.26$	2.82 at 480 nm $b/\lambda_0 = 0.101$ $a/b = 0.10$	1.58 at 530 nm $b/\lambda_0 = 0.162$	2.16 at 620 nm $b/\lambda_0 = 0.178$ $a/b = 0.76$	1.89 at 700 nm $b/\lambda_0 = 0.190$ $a/b = 0.775$

absorption is maximized at neighboring frequencies for nanowires of Al/GaP, Al/AlSb, Au/a-Si, and Ag/Ge, giving polarization-insensitive absorbers. This is not the case for particles of Ag/GaP and Ag/AlSb, where TM absorption is much smaller than TE absorption and follows a decreasing trend with respect to λ_0 [opposite the behavior of TE absorption in the Au/InAs design in Fig. 5(a)]. In addition, one can observe the very high performance of the Ag/GaP core-shell cylinder accompanied by a significant selectivity of frequency, which makes the design suitable for filtering or switching.

IV. HIGHLY SCATTERING DESIGNS

By repeating the procedure described in Sec. II B, we obtain the designs in Table III, which exhibit maximal $P_{scat}/P_{0,scat}$ for each of the polarizations considered. Our metric compares the scattering from the selected core-shell nanoparticle with the scattering of an impenetrable PEC cylinder of radius b and therefore few dielectrics are suitable to compete with such a challenging criterion. Indeed, only AlSb and GaP give large ratios (greater than 1.5), and this can happen even in the absence of metals. When Al/AlSb is considered under TM

illumination, a single AlSb rod ($a/b = 0$ as indicated in Table III) does a better job than all the corresponding variants of Al/AlSb core-shell nanowires; that is why the specific homogeneous AlSb design working at $\lambda_0 = 700$ nm is mentioned twice in Table III. As far as the operating frequencies are concerned, we observe the variety of colors that GaP-coated particles can scatter, while the AlSb claddings always score best for red illumination.

When it comes to the field concentration in the vicinity of the particle under TM excitation, we obtain dipolar patterns similar to those in Fig. 2(a) for the highly scattering structures in Table III. Similarly, the far-field responses resemble those of Huygens sources with moderate back or side lobes and large forward scattering [41], as also happens in the TM-absorbing designs. In Fig. 6(a), we present the magnitude of the magnetic field when the scatterer is the single GaP rod, working for TE illumination at $\lambda_0 = 530$ nm, shown in Table III. Again we notice bipolar resonance [3], which is confined to the semiconducting wire, but this is not the case for the rest of the strong TE scatterers. Their typical signal distribution is shown in Fig. 6(b), where a quadrupole localized surface plasmon resonance [40] appears; the maximal values are recorded
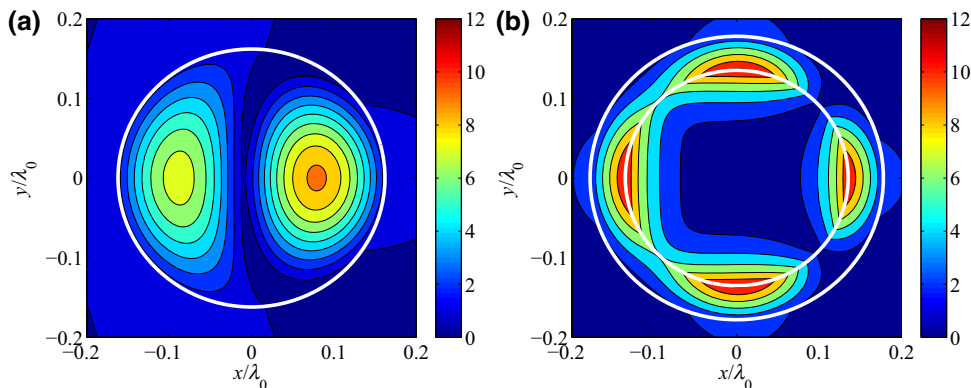

FIG. 6.   Spatial distribution of the magnitude of the normalized sole magnetic component for an optimally-TE-scattering core-shell particle of (a) GaP alone ($\lambda_0 = 530$ nm) and (b) Ag/GaP ($\lambda_0 = 620$ nm).
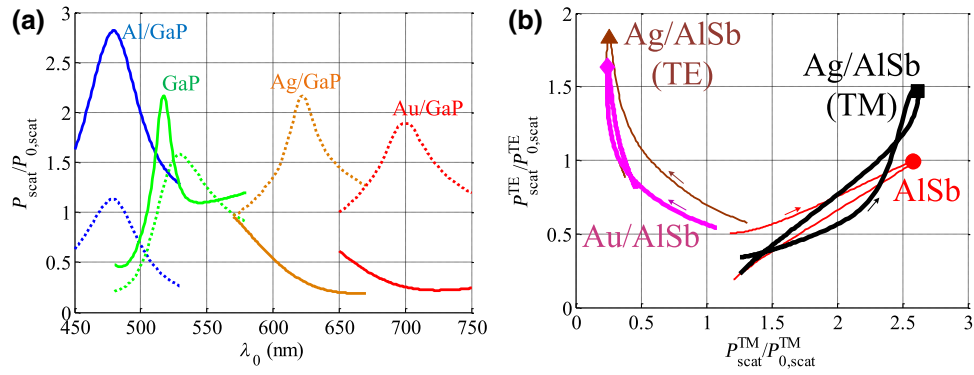
FIG. 7.   (a) Scattering metric $P_{scat}/P_{0,scat}$ for both polarizations as a function of operating wavelength λ_0 of selected GaP-coated optimal designs picked from Table III. Solid lines correspond to the TM response and dashed lines correspond to the TE response. (b) Trajectories on the plane of TM and TE scattering metrics of selected AlSb-coated optimal designs picked from Table III working at $\lambda_0 = 700$ nm (marked) for 600 nm $< \lambda_0 < 800$ nm. The small arrows show the direction of increasing λ_0.

along the y axis and obviously at the points where metal touches the dielectric shell.

In Fig. 7(a), we present the scattering performance for the GaP-based designs in Table III as function of wavelength λ_0 for both polarizations. Obviously, the performance deteriorates far from the optimal frequency but the response to waves with nonoptimized polarization exhibits large variation. In particular, there is a huge spread between the scattering of TE and TM fields by the Al/GaP design, while both curves have similar magnitude for the GaP particle. Furthermore, the TE-scattering designs, do not exhibit substantial capability to scatter the other type (TM) of waves. The AlSb-based designs all operate at the same wavelength ($\lambda_0 = 700$ nm, red) and thus we select them to show their response for both polarizations on the plane of $\left(P_{scat}^{TM}/P_{0,scat}^{TM}, P_{scat}^{TE}/P_{0,scat}^{TE}\right)$ as in Fig. 7(b). In particular, we represent the TM scattering metric along the horizontal axis and the TE one along the vertical axis, while the wavelength λ_0 sweeps the range 600 nm $< \lambda_0 <$ 800 nm; the central value for $\lambda_0 = 700$ nm is marked by different-shaped pointers in each curve. The operation deviates toward either smaller or larger λ_0, but the trend of both metrics is similar; the moderate difference in the behavior for $\lambda_0 < 700$ nm and for $\lambda_0 > 700$ nm can be understood by the small arrows, which indicate the direction of increasing λ_0. The two loci on the right side, which concern TM-optimized designs, give lower performances for both polarizations once we move from the central point. In contrast, in the two lines on the left side (high TE scattering), the metric deteriorates for TE waves and improves for TM waves far from the optimal regime. Such unexpected behavior is attributed to the larger sizes (b/λ_0) and higher plasmonic portions (a/b) of the TE designs, which allow them to adapt their scattering interaction with waves of TM polarization; the same happens for most of the maximally absorbing nanorods in Fig. 5(b).

V. CONCLUSIONS

A simple core-shell nanowire illuminated by visible light is optimized with respect to absorption and scattering efficiency by our testing all possible available material combinations in the presence of realistic losses. Numerous designs with high scores in terms of two different polarizations and for various operating wavelengths are reported, whose performances constitute limits under the assumption of using bulk metals, semiconductors, or dielectrics. Some of them are selected, and from their near-field spatial distributions, far-field radiation patterns, and frequency responses, useful conclusions are reached, such as the different behavior of optimal nanorods when the electric field is oscillating normally or parallel to their axis. In addition, a specific class of hollow plasmonic nanotubes is found to exhibit substantial absorptivity accompanied by abrupt field changes into the shell, while other rods with sharp transfer functions are befitted to sensing or filtering applications.

The approach adopted in this work serves the purpose of inverse design in simple photonic configurations by providing several alternative materializations. The efficiencies recorded may be used as bars for more complicated structures of similar sizes, using more sophisticated media, to pass. The same process can be repeated for other simple particles in various geometries (core-shell nanospheres, planar bilayers) to formulate a primitive library of best designs with respect to multiple objectives in the visible spectrum.

————————

[1] C. F. Bohren and D. R. Huffman, *Absorption and Scattering of Light By Small Particles* (John Wiley & Sons, New York, 1983).

[2] 2014 US Department of Defense MURI Awards, *Control of Light Propagation through Metasurfaces: Active Metasurfaces for Advanced Wavefront Engineering and Waveguiding*, PI: Federico Capasso, www.defense.gov/Portals/1/Documents/pubs/FY14-MURITeamsRecommended.pdf, June 2014.

[3] S. A. Mann and E. C. Garnett, Extreme light absorption in thin semiconductor films wrapped around metal nanowires, Nano Lett. **13**, 3173 (2013).

[4] L. Cao, J. S. White, J. S. Park, J. A. Schuller, B. M. Clemens, and M. L. Brongersma, Engineering light absorption in semiconductor nanowire devices, Nat. Mater. **8**, 643 (2009).

[5] K. Y. Nie, J. Li, X. Chen, Y. Xu, X. Tu, F. F. Ren, Q. Du, L. Fu, L. Kang, K. Tang, S. Gu, R. Zhang, P. Wu, Y. Zheng, H. H. Tan, C. Jagadish, and J. Ye, Extreme absorption enhancement in ZnTe:O/ZnO intermediate band core-shell nanowires by interplay of dielectric resonance and plasmonic bowtie nanoantennas, Sci. Rep. **7**, 7503 (2017).

[6] R. E. Hamam, A. Karalis, J. D. Joannopoulos, and M. Soljacic, Coupled-mode theory for general free-space resonant scattering of waves, Phys. Rev. A **75**, 053801 (2007).

[7] Q. Li, J. B. Wright, W. W. Chow, T. S. Luk, I. Brener, L. F. Lester, and G. T. Wang, Single-mode GaN nanowire lasers, Opt. Express **20**, 17873 (2012).

[8] Z. Ruan and S. Fan, Superscattering of Light from Subwavelength Nanostructures, Phys. Rev. Lett. **105**, 013901 (2010).

[9] L. J. Lauhon, M. S. Gudiksen, D. Wang, and C. M. Lieber, Epitaxial core-shell and core-multishell nanowire heterostructures, Nature **420**, 57 (2002).

[10] X. Xia, J. Tu, Y. Zhang, X. Wang, C. Gu, X. B. Zhao, and H. J. Fan, High-quality metal oxide core/shell nanowire arrays on conductive substrates for electrochemical energy storage, ACS Nano **6**, 5531 (2012).

[11] L. Dou, F. Cui, Y. Yu, G. Khanarian, S. W. Eaton, Q. Yang, J. Resasco, C. Schildknech, K. Schierle-Arndt, and P. Yang, Solution-processed copper/reduced-graphene-oxide core/shell nanowire transparent conductors, ACS Nano **10**, 2600 (2016).

[12] Z. Nie, A. Petukhova, and E. Kumacheva, Properties and emerging applications of self-assembled structures made from inorganic nanoparticles, Nat. Nanotechnol. **5**, 15 (2010).

[13] G. Kaltenpoth, M. Himmelhaus, L. Slansky, F. Caruso, and M. Grunze, Conductive core-shell particles: An approach to self-assembled mesoscopic wires, Adv. Mater. **15**, 1113 (2003).

[14] J. Tang, Z. Huo, S. Brittman, H. Gao, and P. Yang, Solution-processed core-shell nanowires for efficient photovoltaic cells, Nat. Nanotechnol. **6**, 568 (2011).

[15] J. D. Joannopoulos, S. G. Johnson, J. N. Winn, and R. D. Meade, *Photonic Crystals: Molding the Flow of Light* (Princeton University Press, Princeton, 2011).

[16] S. Sandhu and S. Fan, Current-voltage enhancement of a single coaxial nanowire solar cell, ACS Photonics **2**, 1698 (2015).

[17] S.-K. Kim, R. W. Day, J. F. Cahoon, T. J. Kempa, K.-D. Song, H.-G. Park, and C. M. Lieber, Tuning light absorption in core/shell silicon nanowire photovoltaic devices through morphological design, Nano Lett. **12**, 4971 (2012).

[18] V. Jain, M. Heurlin, E. Barrigon, L. Bosco, A. Nowzari, S. Shroff, V. Boix, M. Karimi, R. J. Jam, A. Berg, L. Samuelson, M. T. Borgstrom, F. Capasso, and H. Pettersson, InP/InAsP nanowire-based spatially separate absorption and multiplication avalanche photodetectors, ACS Photonics **4**, 2693 (2017).

[19] R. Hajimammadov, A. Bykov, A. Popov, K. L. Juhasz, G. S. Lorite, M. Mohl, A. Kukovecz, M. Huuhtanen, and K. Kordas, Random networks of core-shell-like $Cu - Cu_2O/CuO$ nanowires as surface plasmon resonance-enhanced sensors, Sci. Rep. **8**, 4708 (2018).

[20] A. Rahimzadegan, C. Rockstuhl, and I. Fernandez-Corbaton, Core-shell Particles as Building Blocks for Systems with High Duality Symmetry, Phys. Rev. Appl. **9**, 054051 (2018).

[21] A. E. Serebryannikov, K. B. Alici, E. Ozbay, and A. Lakhtakia, Thermally sensitive scattering of terahertz waves by coated cylinders for tunable invisibility and masking, Opt. Express **26**, 1 (2018).

[22] G. L. Liu, Y. Yin, S. Kunchakarra, B. Mukherjee, D. Gerion, S. D. Jett, D. G. Bear, J. W. Gray, A. P. Alivisatos, L. P. Lee, and F. F. Chen, A nanoplasmonic molecular ruler for measuring nuclease activity and DNA footprinting, Nat. Nanotechnol. **1**, 47 (2006).

[23] M. N. Gjerding, R. Petersen, T. G. Pedersen, N. A. Mortensen, and K. S. Thygesen, Layered van der Waals crystals with hyperbolic light dispersion, Nat. Commun. **8**, 320 (2017).

[24] M. G. Blaber, M. D. Arnold, and M. J. Ford, Search for the ideal plasmonic nanoshell: The effects of surface scattering and alternatives to gold and silver, J. Phys. Chem. C **113**, 3041 (2009).

[25] O. D. Miller, C. W. Hsu, M. T. H. Reid, W. Qiu, B. G. DeLacy, J. D. Joannopoulos, M. Soljacic, and S. G. Johnson, Fundamental Limits to Extinction by Metallic Nanoparticles, Phys. Rev. Lett. **112**, 123903 (2014).

[26] O. D. Miller, A. G. Polimeridis, M. T. H. Reid, C. W. Hsu, B. G. DeLacy, J. D. Joannopoulos, M. Soljacic, and S. G. Johnson, Fundamental limits to optical response in absorptive systems, Opt. Express **24**, 3329 (2016).

[27] S. Molesky, Z. Lin, A. Y. Piggott, W. Jin, J. Vuckovic, and A. W. Rodriguez, Inverse design in nanophotonics, Nat. Photonics **12**, 659 (2018).

[28] J. Peurifoy, Y. Shen, L. Jing, Y. Yang, F. Cano-Renteria, B. G. DeLacy, J. D. Joannopoulos, M. Tegmark, and M. Soljacic, Nanophotonic particle simulation and inverse

design using artificial neural networks, Sci. Adv. **4,** 6 (2018).

[29] C. A. Valagiannopoulos and P. Alitalo, Electromagnetic cloaking of cylindrical objects by multilayer or uniform dielectric claddings, Phys. Rev. B **85,** 115402 (2012).

[30] C. A. Balanis, *Advanced Engineering Electromagnetics* (John Wiley & Sons, New York, 1989), p. 577.

[31] N. Yu and F. Capasso, Flat optics with designer metasurfaces, Nat. Mater. **13,** 139 (2014).

[32] Z. Tagay and C. Valagiannopoulos, Highly selective transmission and absorption from metasurfaces of periodically corrugated cylindrical particles, Phys. Rev. B **98,** 115306 (2018).

[33] V. O. Byelobrov, T. L. Zinenko, K. Kobayashi, and A. I. Nosich, Periodicity matters: Grating or lattice resonances in the scattering by sparse arrays of subwavelength strips and wires, IEEE Antennas Propag. Mag. **57,** 34 (2015).

[34] http://refractiveindex.info/ (accessed August 21, 2018).

[35] D. E. Aspnes and A. A. Studna, Dielectric functions and optical parameters of Si, Ge, GaP, GaAs, GaSb, InP, InAs, and InSb from 1.5 to 6.0 eV, Phys. Rev. B **27,** 985 (1983).

[36] K. M. McPeak, S. V. Jayanti, S. J. P. Kress, S. Meyer, S. Iotti, A. Rossinelli, and D. J. Norris, Plasmonic films can easily be better: Rules and recipes, ACS Photonics **2,** 326 (2015).

[37] K. Pemasiri, H. E. Jackson, L. M. Smith, B. M. Wong, S. Paiman, Q. Gao, H. H. Tan, and C. Jagadish, Quantum confinement of excitons in wurtzite InP nanowires, J. Appl. Phys. **117,** 194306 (2015).

[38] M. Fickenscher, T. Shi, H. E. Jackson, L. M. Smith, J. M. Yarrison-Rice, C. Zheng, P. Miller, J. Etheridge, B. M. Wong, Q. Gao, S. Deshpande, H. Hoe Tan, and C. Jagadish, Optical, structural, and numerical investigations of GaAs/AlGaAs core-multishell nanowire quantum well tubes, Nano Lett. **13,** 1016 (2013).

[39] J. Greil, S. Assali, Y. Isono, A. Belabbes, F. Bechstedt, F. O. V. Mackenzie, A. Y. Silov, P. A. M. Bakkers, and J. E. M. Haverkort, Optical properties of strained wurtzite gallium phosphide nanowires, Nano Lett. **16,** 3703 (2016).

[40] J. Cao, T. Sun, and K. T. V. Grattan, Gold nanorod-based localized surface plasmon resonance biosensors: A review, Sens. Actuators B Chem. **195,** 332 (2014).

[41] C. A. Valagiannopoulos and S. A. Tretyakov, Symmetric absorbers realized as gratings of PEC cylinders covered by ordinary dielectrics, IEEE Trans. Antennas Propag. **62,** 5089 (2014).

[42] S. Tretyakov, *Analytical Modeling in Applied Electromagnetics* (Artech House, Boston, 2003), p. 205.

[43] E. A. Velichko and A. I. Nosich, Refractive-index sensitivities of hybrid surface-plasmon resonances for a core-shell circular silver nanotube sensor, Opt. Lett. **38,** 4978 (2013).